Quantum Wavepacket Ab Initio Molecular Dynamics: An Approach for Computing Dynamically Averaged Vibrational Spectra Including Critical Nuclear Quantum Effects†

Isaiah Sumner and Srinivasan S. Iyengar*

Departments of Chemistry and Physics, Indiana University, 800 East Kirkwood Avenue, Bloomington, Indiana 47405

Received: June 12, 2007; In Final Form: August 11, 2007

We have introduced a computational methodology to study vibrational spectroscopy in clusters inclusive of critical nuclear quantum effects. This approach is based on the recently developed quantum wavepacket ab initio molecular dynamics method that combines quantum wavepacket dynamics with ab initio molecular dynamics. The computational efficiency of the dynamical procedure is drastically improved (by several orders of magnitude) through the utilization of wavelet-based techniques combined with the previously introduced time-dependent deterministic sampling procedure measure to achieve stable, picosecond length, quantum−classical dynamics of electrons and nuclei in clusters. The dynamical information is employed to construct a novel cumulative flux/velocity correlation function, where the wavepacket flux from the quantized particle is combined with classical nuclear velocities to obtain the vibrational density of states. The approach is demonstrated by computing the vibrational density of states of $[Cl-H-Cl]^-$, inclusive of critical quantum nuclear effects, and our results are in good agreement with experiment. A general hierarchical procedure is also provided, based on electronic structure harmonic frequencies, classical ab initio molecular dynamics, computation of nuclear quantum−mechanical eigenstates, and employing quantum wavepacket ab initio dynamics to understand vibrational spectroscopy in hydrogen-bonded clusters that display large degrees of anharmonicities.

I. Introduction

The impact of hydrogen-bonded systems and hydrogen transfer extends beyond fundamental chemistry and well into the areas of materials,[1−5] atmospheric,[6−13] condensed,[14−17] and gas-phase cluster chemistry,[10−13,18−20] and biological sciences.[21−23] Recently, gas-phase single-photon[24] and multiphoton[25] vibrational action spectroscopy experiments and condensed-phase multidimensional infrared experiments[26,27] have become critical in deciphering the precise vibrational signatures that contribute to dynamics in soft-mode hydrogen-bonded systems. In biological systems, many enzymes that catalyze hydrogen-transfer reactions are thought to display tunneling.[21] Proton-transfer reactions are also of interest in fuel cell applications.[1]

However, there are multiple factors that influence the accurate computational modeling of processes involving excess protons, hydride ions, and atomic hydrogen in heterogeneous systems. For protons and hydride ions, the polarizability of the immediate environment[19] and the changing bonding topography during a transfer process[11,13] render the problem attractive to ab initio quantum chemical treatment. Dynamical aspects become significant at finite temperatures,[9−11] and nuclear quantum effects may be critical through hydrogen tunneling and zero-point effects.[19,20]

There exists a number of computational methods that attempt to solve the vibrational spectroscopic problems in such fundamental chemical systems. One of the most direct approaches is through harmonic analyses of optimized nuclear configurations available in standard electronic structure packages. This approach, however, is not adequate for fluxional protonated[11,13] and hydroxide-rich systems.[9,10,20] The effect of nuclear dynamics must be considered through quantum,[28−62] semiclassical,[30,63−78] or classical treatments where the electronic structure is accurately computed.[63,79−86] There are many important methods[29,33,87,88] for the quantum dynamical treatment of nuclei. Some of the bottlenecks in these approaches include the exponential scaling of quantum dynamics and the choice of the coordinate system.[89−91] Recently, several attempts have been made to circumvent the exponential scaling problem numerically,[29,33,34,70,87,88,92−94] and the choice of coordinate systems has also received considerable attention in the literature.[91,90,95,96]

For systems with more than a few degrees of freedom, a classical or semiclassical approximation of nuclei is generally desirable, if only to keep the computational expense tractable. In this regard, for some larger-sized water clusters, a classical treatment of nuclei has been found to be sufficient in providing vibrational properties in agreement with experiments.[11−13] Important insights have been gleaned from these simulations.[11,12] Furthermore, our group has recently contributed a methodology[97−99] that is extended in this publication to treat vibrational spectroscopy in clusters inclusive of critical nuclear quantum effects. Our approach is quantum−classical [69,100−106] and combines a quantum wavepacket dynamics treatment of the time-dependent Schrödinger equation with ab initio molecular dynamics. Consequently, this method is called quantum wavepacket ab initio molecular dynamics (QWAIMD). The approach is summarized below, and details can be found in refs 97−99.

Starting from the time-dependent Schrödinger equation, a system is partitioned into three sections based on chemical

† Part of the special issue "Robert E. Wyatt Festschrift".

* Author to whom correspondence should be addressed. E-mail: iyengar@indiana.edu.

10.1021/jp074522d CCC: $37.00
Published on Web 09/26/2007

complexity.[30,75−77] Subsystem A comprises particles, such as protons, that display critical quantum dynamical effects and is treated as a quantum wavepacket. Subsystems B and C comprise the surrounding "bath'' particles that dynamically influence the properties of subsystem A. We include the bulk of the nuclear and electronic degrees of freedom within subsystems B and C. Ab initio molecular dynamics (AIMD)[63,79−83,85] is used to treat the evolution of these subsystems, where the nuclei in subsystem B are treated using classical mechanics. Both extended Lagrangian[81,83,84,107−111] and Born−Oppenheimer treatment[82,85,86] options are available. We have derived and tested a scheme [97−99] that allows simultaneous dynamics of all three subsystems coupled through a time-dependent procedure. A few salient features of QWAIMD are: (a) The quantum dynamical propagation is formally exact and computationally efficient, because the quantum propagator is represented as a banded Toeplitz matrix.[97−99] (b) The ab initio dynamics treatment allows the use of both accurate (hybrid) density functionals as well as post-Hartree−Fock methods for smaller systems. (c) One of the primary bottlenecks in QWAIMD is the computation of the interaction potential between the quantum wavepacket and the surrounding classical nuclei and electrons. Improvements in efficiency (by several orders of magnitude) are achieved through a novel, time-dependent, deterministic sampling (TDDS)[99] procedure that allows efficient, "on-the-fly'' quantum propagation and simultaneous ab initio dynamical treatment of medium-sized systems.[99] (d) The overall computational scheme for conducting QWAIMD[97−99] displays high efficiency and is implemented in parallel. Time scales on the order of picoseconds are accessible. (e) For periodic condensed-phase systems, wavepacket propagation is being extended through the introduction of a space-group-symmetry-adapted form of the quantum free propagator.[112] QWAIMD has been recently utilized to study quantum mechanical tunneling in enzyme active sites.[113]

This paper is organized as follows: For convenience, the dynamics formalism is briefly reviewed in section II, and further computational generalizations are provided in section III. These generalizations include a Haar wavelet[114−117] implementation of TDDS[99] in section IIIA and a scheme to compute the classical nuclear forces using Lagrange interpolation attenuated by low-pass filtering[118] in section IIIB. In section IV, numerical tests are provided. In section V, a demonstration of the approach is undertaken to predict vibrational spectra in a small $[Cl-H-Cl]^-$ system including critical nuclear quantum effects. This section includes comparisons between frequencies obtained from electronic structure, classical AIMD, and one- and three-dimensional QWAIMD. For the QWAIMD simulations, a new formalism is utilized[99] that includes the cumulative time correlation of the wavepacket flux combined with the velocity or dipole correlation of the classical nuclei. It is noted that the harmonic analysis even at very high levels of electronic structure theory (such as coupled cluster) is insufficient to describe this problem. Classical AIMD is seen to improve on the harmonic result, and QWAIMD provides good agreement with experiment. An analysis of errors is provided by comparing the classical and quantum−classical nuclear dynamics formalisms utilizing the Bohmian quantum potential.[34,105,106,119−126] Conclusions are given in section VI.

II. Quantum Wavepacket Ab Initio Molecular Dynamics Enhanced by Time-Dependent Deterministic Sampling

The QWAIMD approach has been discussed in many recent publications.[97−99] We present a brief summary here. As stated in the Introduction, subsystem A, which comprises particles, such as protons, that display critical quantum dynamical effects obeys

$$\imath\hbar\frac{\partial}{\partial t}\chi(R_{QM};t) = \left[-\frac{\hbar^2}{2M_{QM}}\nabla_{R_{QM}}{}^2 + E(\mathbf{R}_C,R_{QM})\right]\chi(R_{QM};t) \quad (1)$$

Subsystems B and C comprise the surrounding nuclei and electrons that dynamically influence subsystem A and are treated simultaneously using ab initio molecular dynamics.[63,70,79−86,127] Thus subsystem B obeys

$$M\frac{d^2\mathbf{R}_C}{dt^2} = -\left\langle\chi\left|\frac{\partial E(\mathbf{R}_C,R_{QM})}{\partial\mathbf{R}_C}\right|_{\mathbf{P}_C}\right|\chi\right\rangle \quad (2)$$

Here $\chi(R_{QM};t)$ represents the quantum dynamical wavepacket, M_{QM} depicts the mass of the quantum subsystem particle(s) with coordinates R_{QM}, and M denotes the classical nuclear masses with coordinates $\mathbf{R}_C$. Subsystem B experiences an "averaged'' force[128] that depends on the instantaneous wavepacket χ. The non-Hellmann−Feynman contributions to the force rigorously approach zero because $|\chi\rangle$ is obtained from propagation according to eq 1. The electronic structure energy, E, and gradients may be computed using single-particle formalisms such as density functional theory (DFT), Hartree−Fock, or semiempirical treatments for medium-sized systems.[97,99] Post-Hartree−Fock formalisms can currently be utilized for smaller systems with QWAIMD.

An alternative description of subsystems B and C is obtained by employing the recently developed atom-centered density matrix propagation (ADMP) formalism.[83,108−111,129,130] To arrive at this step, we first note that under conditions of "adiabatic control''[84,109,110,131] extended Lagrangian formalisms[132,133] such as ADMP provide good approximations to single-particle (Hartree−Fock, DFT, and semiempirical treatments) Born−Oppenheimer molecular dynamics (BOMD).[11,13,109] When ADMP is used to describe the dynamics of the electrons, subsystem C is described through propagation of the single-particle electronic density matrix, $\mathbf{P}_C$, as

$$\underline{\mu}^{1/2}\frac{d^2\mathbf{P}_C}{dt^2}\underline{\mu}^{1/2} = -\left\langle\chi\left|\frac{\partial E(\{\mathbf{R}_C,\mathbf{P}_C\},R_{QM})}{\partial\mathbf{P}_C}\right|_{\mathbf{R}_C}\right|\chi\right\rangle - [\Lambda\mathbf{P}_C + \mathbf{P}_C\Lambda - \Lambda] \quad (3)$$

Here, $\underline{\mu}$ is a fictitious inertia tensor[83,108−110] describing the motion of $\mathbf{P}_C$, and Λ is a Lagrangian multiplier matrix used to impose N-representability of $\mathbf{P}_C$. The equations of motion for subsystem B remain the same as those in eq 2 apart from the fact that the forces used in ADMP are different from that in BOMD[83,110] through the inclusion of an additional term that depends on the commutator of the single-particle electronic Hamiltonian (Fock matrix) and $\mathbf{P}_C$.

All calculations in this contribution are performed using converged electronic structure calculations (BOMD).

The time evolution of χ is approximated using the symmetric split operator technique,[37,134−136] where the free propagation is carried out in the coordinate representation using distributed approximating functionals (DAFs).[97,98,137,138] The banded Toeplitz representation of the DAF propagator renders a great deal of efficiency to quantum propagation.[59,97,98,137] The evolution of $\{\mathbf{R}_C,\mathbf{P}_C\}$ is given by the velocity Verlet integrator,[139] which is also obtained through a third-order Trotter factorization of the classical Liouville form of the AIMD equations.[97]

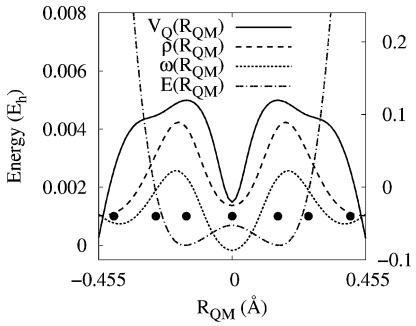

Figure 1. TDDS function, $\omega(R_{QM})$, in comparison with the wavepacket density, $\rho(R_{QM})$, the shifted potential energy surface (shifted such that the minimum energy point is zero), $E(R_{QM})$, and the Bohmian potential, $V_Q(R_{QM}) \equiv -(\hbar^2/2m)(1/\sqrt{\rho})\nabla^2\sqrt{\rho}$ at one time slice from a one-dimensional dynamical treatment of the shared proton in $[Cl-H-Cl]^-$. The wavepacket is localized in two areas where the potential energy is low. Therefore, $\omega(R_{QM})$ has a higher density in these areas, resulting in a higher density of calculations. The left vertical axis represents $E(R_{QM})$, while the right vertical axis represents $V_Q(R_{QM})$.

An important advantage of QWAIMD is that the potential energy surface in eq 1 is obtained on-the-fly during dynamics, which obviates the need for an a priori fitted electronic surface. However, the need to compute an approximation to the time-dependent energy and gradients, at every time step, constitutes a computational bottleneck in the procedure, and the complexity grows linearly with the number of grid points. Hence, the number of grid points where the electronic structure energy and gradients are evaluated needs to be optimized to bring the overall scaling of the algorithm down from a dependence on the total number of quantum dynamical grid points to a small fraction where the electronic structure calculations are performed. Toward this, we introduced a TDDS measure in ref 99 that adaptively helps determine the relevant regions of the potential where the energy and gradients are obtained; the values of these parameters in the other regions are obtained through an efficient interpolation scheme. The TDDS function is defined as

$$\omega(R_{QM}) \propto \frac{[\tilde{\rho} + 1/I_\chi][\tilde{E}' + 1/I_{E'}]}{\tilde{E} + 1/I_E} \tag{4}$$

where $\tilde{\rho}$, $\tilde{E}'$, and $\tilde{E}$ are the L^∞-normalized wavepacket, gradient ($E' \equiv [\partial E(\{\mathbf{R}_C,\mathbf{P}_C\},R_{QM})/\partial R_{QM}]$), and potential energy.[99] The parameters, I_χ, $I_{E'}$, and I_E are chosen to be integers and are fixed at values that yield an equal distribution of grid points in the classically allowed (minimum energy) and classically forbidden (in the vicinity of the classical turning point) regions of the potential surface. The sampling function is evaluated at every instant in time to help determine the grid points where the potential and gradient evaluations are conducted. In section III we present new algorithms to implement the TDDS, and in section IV we find that a reduction in computational effort of several orders of magnitude is achieved via the sampling function and the numerical implementation developed in section III.

In Figure 1, the TDDS function is illustrated along with the wavepacket, the shifted potential energy surface, and the Bohmian quantum potential,[119] $V_Q(R_{QM}) = -(\hbar^2/2m)(1/\sqrt{\rho})\nabla^2\sqrt{\rho}$, at one time slice from a QWAIMD treatment of $[Cl-H-Cl]^-$ where the shared proton is a one-dimensional wavepacket. The Bohmian quantum potential represents regions of the surface where quantum mechanical contributions are important. It has been shown in ref 99 that the TDDS function exhibits significant contributions in regions around wavepacket nodes, where the Bohmian potential is large. In Figure 2, we also present the behavior of the time-averaged TDDS function and the Bohmian quantum potential at two different temperatures. At the higher temperature, the wavepacket penetrates deeper into the barrier, which is seen from the broader distribution of ρ in Figure 2a. The deeper penetration is facilitated by a larger average kinetic energy of the wavepacket at the classical turning point, that is, a more oscillatory nature of χ, which translates to the oscillatory nature of the Bohmian potential beyond the turning point for the higher-temperature simulation. The time-averaged TDDS function tracks the time-averaged Bohmian potential in regions where the wavepacket amplitude is significant. (Compare $\langle\omega(R_{QM})\rangle$ in both plots to notice the broader spread into the classically forbidden region for the higher-temperature simulation.) This aspect has important bearings on our results in section V where we notice a temperature dependence to the vibrational spectrum. This temperature dependence is a direct consequence of the discussion here, i.e., the greater penetration of the wavepacket facilitated by the broader Cl−Cl distribution at higher temperatures.

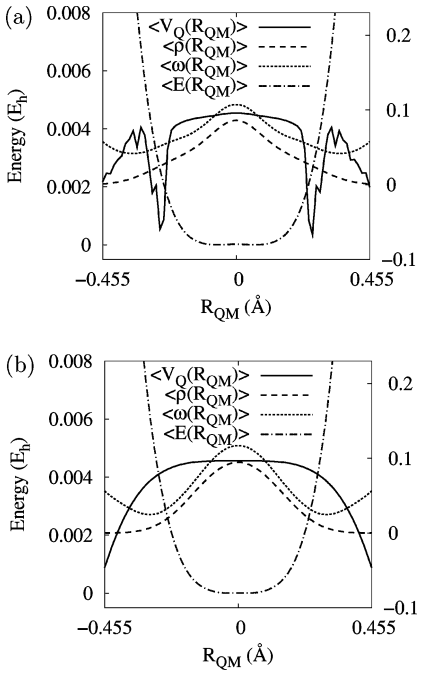

Figure 2. Time-averaged TDDS function, $\langle\omega(R_{QM})\rangle$, wavepacket density, $\langle\rho(R_{QM})\rangle$, classical potential, $\langle E(R_{QM})\rangle$, and Bohmian potential energy surface, $\langle V_Q(R_{QM})\rangle$. The time-averaged Bohmian potential tracks the time-averaged TDDS function well in areas with a significant wavepacket density. Panel a shows a high-temperature simulation (T = 271.14 K), and panel b shows a low-temperature simulation (T = 133.76 K) of $[Cl-H-Cl]^-$ (see text). In both panels, the left vertical axis represents $E(R_{QM})$, whereas the right vertical axis represents $V_Q(R_{QM})$.

III. Computational Algorithms for Quantum Wavepacket Ab Initio Molecular Dynamics Using Time-Dependent Deterministic Sampling

Apart from the $\mathcal{O}(\Delta t^3)$ errors introduced using the symmetric split operator and the velocity Verlet schemes, the error in wavepacket propagation is directly proportional to that introduced from computing the potential on a discrete set of grid points. If $\Delta E(R_{QM})$ is the (time-dependent) error introduced in the potential as a result of TDDS, then the deviation of the propagated wavepacket, from the exact result, is proportional

to $\Delta E(R_{QM})$, and to allow the computational dynamics to be close to the exact result, this quantity should remain small. To provide an adaptive control on the accuracy of the dynamics, we present two sets of algorithms. In section IIIA, we compute the "ideal'' set of grid points, where electronic structure calculations are performed, using a wavelet representation of TDDS. This scheme, along with Lagrange interpolation attenuated by low-pass filter functions,[118] is then used in section IIIB to compute the forces on the classical nuclei.

A. A Haar Wavelet Representation of the Time-Dependent Deterministic Sampling Function. We wish to perform quantum dynamics on a grid comprising N_Q points using electronic structure energies and gradients computed only at N_E points ($N_E \ll N_Q$), determined using the TDDS function in eq 4. Some algorithms for reduced dimensional cases have been introduced in ref 99. However, these algorithms do not utilize the full anisotropy and dimensional dependence of the TDDS function, ω. Here, we generalize these algorithms through the construction of a multiresolution analysis[114,116,117,140,141] of ω. Let us first consider the following definitions for the scaling and wavelet functions used to construct multiresolution analysis

$$\xi_{i,j}(x) = a^{-j/2}\xi(xa^{-j} - i) \tag{5}$$

$$\eta_{i,j}(x) = a^{-j/2}\eta(xa^{-j} - i) \tag{6}$$

where $\xi(x)$ is the scaling function and is generally localized in lower-frequency regions, while $\eta(x)$ is the wavelet function and has relatively greater high-frequency components.[114,116,117,140−142] Using the translation−dilation properties of eqs 5 and 6, an overcomplete hierarchy of basis functions is constructed. The indices i and j are generally integers, although that is not required. The quantity a specifies the extent of "dilation''. In most signal processing applications, the two-scale version ($a = 2$) of these equations is common[141] but not so in standard electronic structure.[167] On the basis of eqs 5 and 6, a variety of hierarchical wavelet bases have been developed.[111,115,117,142−145]

Here, we expand the multidimensional, positive semidefinite TDDS function as a multiconfigurational (sum-of-products) expansion of Haar scaling functions

$$\omega(R_{QM}) \propto \frac{[\tilde{\rho} + 1/I_\chi][\tilde{E}' + 1/I_{E'}]}{\tilde{E} + 1/I_E} = \sum_{i=0}^{N_{GEN}} \underline{\sum_{j_1=0}^{a^i-1} \cdots \sum_{j_{N_{Dim}}=0}^{a^i-1}} c_{i,\{j\}} \left\{ \prod_{k=1}^{N_{Dim}} \mathscr{H}\left(a^i R_{QM}^k - \frac{j_k N_Q}{a^i} \right) \right\} \tag{7}$$

where the Haar scaling function, $\mathscr{H}(x)$, is a square function equal to 1, for $0 \le x \le 1$, and zero otherwise. The quantity N_{GEN} is the number of wavelet generations, and the underline below the summations is meant to indicate that there are N_{Dim} summations, $[j_1, j_2, ..., j_{N_{Dim}}]$, and $c_{i,\{j\}}$ implies that the coefficients depend on i and the entire set of j-indices. The functions $\{\mathscr{H}(a^i x - j_k N_Q/a^i)\}$ comprise a hierarchy of translated and dilated forms of $\mathscr{H}(x)$. We only use the scaling function in our treatment because the Haar wavelet function is the orthogonal complement of the Haar scaling function and is not positive semidefinite. (The TDDS function is required to be positive semidefinite.) The quantity R_{QM}^k, in eq 7, is the kth component of the N_{Dim}-dimensional vector, and a is chosen to be 2 or 3; that is, we employ two- and three-scale functions in our scheme.

The family of functions $\{\mathscr{H}(a^i R_{QM}^k - j_k N_Q/a^i)\}$ for all allowed values of indices i, j_k, and k, form an overcomplete nonorthogonal set of functions for different i values. The algorithm picks an orthogonal subset with coefficients in this series determined according to the constraint $\langle \Pi_{k=1}^{N_{Dim}} \mathscr{H}(a^i R_{QM}^k - j_k N_Q/a^i) | \omega(R_{QM}) \rangle \equiv c_{i,\{j\}} \approx 1$. Because the TDDS function ω has the physical interpretation that $[\omega(x)dx]$ is the number of electronic structure calculations to be performed inside the volume dx, $c_{i,\{j\}}$ represents the number of calculations to be performed inside the physical region defined by the Haar scaling function $[\Pi_{k=1}^{N_{Dim}} \mathscr{H}(a^i R_{QM}^k - j_k N_Q/a^i)]$. This implies that one electronic structure calculation (energy and forces) needs to be performed inside the region defined by every wavelet given by the indices i, j_k, and k where the coefficient is equal to 1. It is also important to note that the reduced grid obtained from this scheme is not a direct product grid.

B. Classical Nuclear Forces through Lagrange Interpolation Attenuated by Low-Pass Filtering. The QWAIMD approach requires the time-dependent potential and gradients on a set of N_Q grid points. In section IIIA, we introduced a computational algorithm that utilizes wavelet theory to represent the TDDS function and hence perform electronic structure calculations on a potentially smaller set of grid points. In this section, we discuss approaches to estimate the average forces, $\langle \chi | (\partial E(\{\mathbf{R}_C, \mathbf{P}_C\}, R_{QM})/\partial \mathbf{R}_C)|_{\mathbf{P}_C} | \chi \rangle$, using the electronic structure gradients at the set $\{i\}$ of N_E grid points. The simplest algorithm utilizes an irregular grid summation

$$\left\langle \chi \left| \left. \frac{\partial E(\{\mathbf{R}_C, \mathbf{P}_C\}, R_{QM})}{\partial \mathbf{R}_C} \right|_{\mathbf{P}_C} \right| \chi \right\rangle \approx \sum_i^{N_E} \left. \frac{\partial E(\{\mathbf{R}_C, \mathbf{P}_C\}, R_{QM}^i)}{\partial \mathbf{R}_C} \right|_{\mathbf{P}_C} \rho(R_{QM}^i) b_i^{Trpz} \tag{8}$$

where $\rho(R_{QM}^i) = \chi^*(R_{QM}^i)\chi(R_{QM}^i)$ and the volume element b_i^{Trpz} is obtained from trapezoidal rule.

A second procedure that we have tested for force estimation is through low-pass filtered Lagrange interpolation[118]

$$\left\langle \chi \left| \left. \frac{\partial E(\{\mathbf{R}_C, \mathbf{P}_C\}, R_{QM})}{\partial \mathbf{R}_C} \right|_{\mathbf{P}_C} \right| \chi \right\rangle \approx \sum_i^{N_E} \left. \frac{\partial E(\{\mathbf{R}_C, \mathbf{P}_C\}, R_{QM}^i)}{\partial \mathbf{R}_C} \right|_{\mathbf{P}_C} b_i^{Lag-LPF} \tag{9}$$

where

$$b_i^{Lag-LPF} = \int \prod_{j=1}^{N_{Dim}} dx_j \zeta(x_j - x_j^i) P_i(x_j) \rho(x_j) \tag{10}$$

The P_i are one-dimensional Lagrange interpolating polynomials, and the functions ζ are low-pass filter functions;[118] we use a Gaussian function in the current study to represent ζ; however, that is not the only possible choice. We use low-pass filtering here because it is well-known that Lagrange interpolation can introduce spurious high frequencies into the functional fit.[146] Clearly the differences between eqs 8 and 9 arise from the fact that the grid sample, b_i in eq 9, is smooth. Other grid samples will be tested in future publications.

TABLE 1: Energy Conservation Summary for Cl−H−Cl⁻ [a]

	N_E	N_Q	N_Q/N_E	time (ps)	ΔE (hartree)
1D-QWAIMD[b]	11[c]	101	9.18	3.0	1.3×10^{-5}
	11[d]	101	9.18	2.4	2.3×10^{-5}
3D-QWAIMD[e]	1331	210681	158	0.4	4.5×10^{-5}
	441	210681	478	0.7	7.9×10^{-5}
	441	232897	528	0.7	3.5×10^{-5}
	343	232897	679	1.4	4.5×10^{-5}
	64	232897	3639	0.4	6.7×10^{-4}

[a] N_Q is the total number of grid points, and N_E is the actual number of calculations performed, placed (irregularly) on the grid employing the Haar wavelet implementation of TDDS. Thus, the ratio N_Q/N_E represents the computational gain. ΔE represents the standard deviation of the total (kinetic plus potential) energy of the system during the simulation. [b] The 6-31+G(d,p) basis is used for one-dimensional studies. [c] On-the-fly electronic structure is performed using the B3LYP density functional. [d] On-the-fly electronic structure is performed using MP2. [e] The B3LYP/6-31+G* level of theory is used for three-dimensional QWAIMD studies.

IV. Numerical Tests on Accuracy and Efficiency of Wavelet-Based TDDS and the Force Estimation Algorithm

We have chosen to study a bihalide cluster, $[Cl-H-Cl]^-$, to benchmark our approach. This has been the subject of substantial experimental and theoretical study[147−154] and contains a shared proton undergoing excursions between donor−acceptor moieties. Hence, it is foreseeable that the shared proton modes may be coupled with all other atoms. Furthermore, due to the size of the problem (three atoms), it is possible to treat this system using full-dimensional quantum dynamics. Our goal here, instead, is to gauge the accuracy of our quantum−classical dynamical scheme for electrons and nuclei, and hence, in our study, the shared proton is treated using quantum dynamics whereas all other atoms are treated with BOMD, as allowed within QWAIMD. The electronic structure is treated using DFT, Hartree−Fock, and post-Hartree−Fock MP2 formalisms. All QWAIMD computations in this publication are performed using a development version of the Gaussian series[155] of electronic structure codes.

Table 1 provides a summary of the one- and three-dimensional wavepacket numerical tests. Further details can be found in Tables 2 and 3, but it is already clear that 1 order of magnitude compression in grid size is possible through TDDS when a one-dimensional quantum treatment is utilized and 3−4 orders of magnitude of compression in grid size is possible when the wavepacket is treated in full three dimensions. Because the potential and gradient evaluations are the critical bottlenecks in QWAIMD, this leads to a large reduction in computational time.

In Tables 2 and 3, we analyze the energy conservation properties of the dynamics over a range of N_E values for different initial conditions (simulation temperatures and initial wavepackets), electronic structure methodologies, classical nuclear force calculation algorithms, and dimensionalities of the quantum mechanical particle. The initial wavepacket is chosen as a linear combination of the proton Hamiltonian eigenstates at the initial time step

$$\chi_0 = \sum c_i \phi_i \tag{11}$$

where the eigenstates ϕ_i (and the corresponding eigenvalues E_i) are obtained from Arnoldi iterative diagonalization of the proton Hamiltonian at the initial step.[156−158] The Arnoldi scheme is a variant of the Lanczos method[156−158] and involves the repetitive application of the Hamiltonian matrix on an initial vector to form a Krylov basis set.[156] The representation of the Hamiltonian in this new basis set leads to a Hessenberg form or tri-diagonal form[156] for the Hamiltonian, which is relatively easy to diagonalize. Note from Table 3 that the size of the matrices involved, given by N_Q, can be very large, which explains the need for employing the iterative diagonalization scheme. The coefficients in eq 11 are obtained in two different ways, leading to two different families of initial wavepackets for the tests shown in Tables 2 and 3. In one case, a thermalized initial wavepacket is obtained usingwhere β is inverse temperature.

TABLE 2: Energy Conservation Data from a One-Dimensional Dynamical Treatment of the Shared Proton in [Cl−H−Cl]⁻ [a]

level of theory	χ_0	force scheme	temperature (K)[b]	N^E	N_Q/N_E	time (ps)	ΔE (hartree)
HF	eq 13	eq 8	325.26	101	1	1.5	4.8×10^{-5}
B3LYP	eq 13	eq 8	258.45	101	1	1.1	1.3×10^{-5}
B3LYP	eq 12	eq 9[c] {41}	134.29	11	9.18	1.3	6×10^{-6}
B3LYP	eq 12	eq 9[c] {53}	134.16	11	9.18	1.7	8×10^{-6}
B3LYP	eq 12	eq 9[c] {62}	134.77	11	9.18	1.0	4.8×10^{-6}
B3LYP	eq 12	eq 9[d]	133.76	11	9.18	3.0	1.3×10^{-5}
B3LYP	eq 13	eq 9[d]	271.14	11	9.18	3.9	1.3×10^{-4}
HF	eq 13	eq 9[d]	321.38	11	9.18	0.5	1.5×10^{-5}
MP2	eq 12	eq 9[d]	127.26	11	9.18	2.4	2.3×10^{-5}
MP2	eq 13	eq 9[d]	290.17	11	9.18	3.7	2.1×10^{-4}
B3LYP	eq 12	eq 8	134.76	11	9.18	1.25	2×10^{-5}
B3LYP	eq 13	eq 8	260.50	11	9.18	1.0	4.4×10^{-5}

[a] For all calculations the quantum dynamical time step, $\Delta t_{QM} = 0.05$ fs, the classical time step, $\Delta t_{Cl} = 0.25$ fs, and $N_Q = 101$. The ratio N_Q/N_E represents the computational gain, and ΔE is the standard deviation of the total energy of the system. The 6-31+G(d,p) basis set was used for all levels of theory. [b] Calculated from classical nuclear velocities and wavepacket kinetic energy. [c] $\zeta(x - x')$ in eq 10 is a Gaussian. The full width at half-maximum is shown in curly brackets (in units of grid points). [d] $\zeta(x - x') = 1$ in eq 10.

TABLE 3: Energy Conservation Data for Cl−H−Cl⁻ for All TDDS Algorithms and Different Force Schemes[a]

χ_0	force scheme	temperature (K)[b]	N_E	N_Q	N_Q/N_E	time (ps)	$\Delta E(E_H)$
eq 12	eq 9[c] {53}	323.50	343	232897[d]	679	1.4	4.5×10^{-5}
eq 12	eq 9[c] {53}	319.40	441	232897[d]	528	0.7	3.5×10^{-5}
eq 12	eq 9[c] {53}	370.03	64	232897[d]	3639	0.4	6.7×10^{-4}
eq 13	eq 9[c] {53}	714.45	343	232897[d]	679	1.9	1.2×10^{-4}
eq 13	eq 9[c] {53}	723.40	441	232897[d]	528	0.7	1.4×10^{-4}
eq 13	eq 9[c] {53}	724.20	441	210681[e]	478	0.7	7.9×10^{-5}
eq 13	eq 9[c] {53}	727.76	1331	210681[e]	158	0.4	4.5×10^{-5}
eq 13	eq 9[c] {41}	719.81	343	232897[e]	679	1.3	1.1×10^{-4}
eq 13	eq 9[f]	726.16	343	232897[f]	679	0.5	2.7×10^{-4}
eq 13	eq 9[d]	904.31	441	232897[f]	528	0.5	1.7×10^{-3}
eq 13	eq 9[d]	770.09	441	210681[e]	478	0.5	3.0×10^{-4}
eq 13	eq 8	709.77	441	210681[e]	478	0.7	2.8×10^{-4}
eq 13	eq 8	715.44	1331	210681[e]	158	0.3	1.3×10^{-4}
eq 13	eq 8	714.771	441	232897[d]	528	0.6	2.3×10^{-4}

[a] All calculations are performed using a three-dimensional dynamical treatment of the shared proton in $[Cl-H-Cl]^-$: 3D-QWAIMD with density functional and basis set B3LYP/6-31+G*. For all calculations, $\Delta t_{QM} = 0.05$ fs and $\Delta t_{Cl} = 0.25$ fs. The ratio N_Q/N_E represents the computational gain, and ΔE represents the standard deviation of the total energy of the system during the simulation. [b] Calculated from classical nuclear velocities and wavepacket kinetic energy. [c] $\zeta(x - x')$ in eq 10 is a Gaussian. The full width at half-maximum is shown in curly brackets (in units of grid points) [d] $97 \times 49 \times 49$ grid with 97 grid points along the Cl−Cl axis. [e] $81 \times 51 \times 51$ grid with 81 grid points along the Cl−Cl axis. [f] $\zeta(x - x') = 1$ in eq 10.

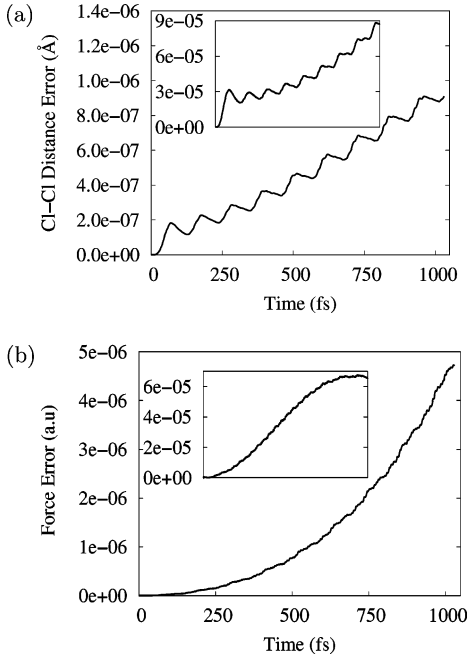

Figure 3. (a) Error in the Cl−Cl distance in a one-dimensional QWAIMD, B3LYP/6-31+G(d,p) simulation of $[Cl-H-Cl]^-$ for $N_E = 11$ with reference to $N_Q = 101$. The initial quantum wavepacket is a Gaussian. (b) Root-mean-square deviation of the classical nuclear forces for the $N_E = 11$ calculation. Clearly, using 11 points in one dimension based on TDDS leads to no significant change in the dynamics over picosecond time scales. The insets in both panels represent force interpolation according to eq 8 while the larger plots display Lagrange interpolation in eq 10. (The difference between the trajectories calculated by the Lagrange polynomial formalisms, with and without low-pass filtering, is indistinguishable in these plots.) The horizontal axes on the insets depict the same time scale as the larger plots. The errors are negligible, but the Lagrange interpolated force formalisms result in a trajectory that is orders of magnitude better than the simple force calculation of eq 8.

$$c_i = \exp[-\beta E_i] \tag{12}$$

In another case a Gaussian initial wavepacket is chosen and hence

$$c_i = \left\langle \phi_i \middle| \exp\left\{\frac{\mathbf{x} - \mathbf{x}_0}{2\alpha^2}\right\} \right\rangle \tag{13}$$

While the thermalized wavepacket, eq 12, allows for eigenstates to be populated starting from the lowest states, the Gaussian distribution, eq 13, allows a different range of eigenstates (generally higher in energy) to be populated because the potential is generally not harmonic. We have used both of these in benchmarking our approach.

Table 2 comprises results from one-dimensional wavepacket dynamics. This allows us to compare the different force estimation algorithms, as discussed in section IIIB. As can be seen, the filtered Lagrange polynomial formalism allows the greatest stability in the dynamics by providing energy conservation in the range of microhartrees for reasonably long (picosecond length) simulations. This fact is also clear from Figure 3 where the error in nuclear forces and deviations in classical chloride dynamics are shown over a picosecond time scale. The agreement is good between the TDDS trajectory and the trajectory obtained from calculations at all N_Q grid points.

Table 3 also indicates good energy conservation for the cases where the filtered Lagrange force interpolation scheme is used in conjunction with the wavelet scheme even for large temperature simulations. The approaches provide a 3−4 orders of magnitude reduction in computational cost (the N_Q/N_E ratio in Tables 2 and 3). Because the temperatures in Table 3 are higher than those in Table 2, the energy conservation is generally of lower quality in Table 3. However, as shown in section V, there is little influence in comparison with measured properties such as vibrational spectra. Also note that the largest compression $N_Q/N_E = 3639$, which is only 64 calculated grid points in three dimensions, may reflect the lower limit for N_E using the current algorithm.

TABLE 4: Vibrational Frequencies at Optimized Geometries[a]

level of theory	ν_1 (cm^{-1})	ν_2 (cm^{-1})		ν_3 (cm^{-1})		Cl−Cl distance (Å)
B3LYP/6-31+G(d,p)	328	834[b]	849[c]	560[b]	949[c]	3.15
B3LYP/aug-cc-PVTZ	324	818[b]	829[c]	582[b]	952[c]	3.15
MP2/6-31+G(d,p)	353	893[b]	907[c]	98[b]	865[c]	3.10
MP2/aug-cc-PVTZ	345	847[b]	863[c]	637[b]	974[c]	3.11
CCSD/aug-cc-PVTZ	181	828[b]	874[c]	833[b]	764[c]	3.14[d]
CCSD(T)/aug-cc-PVTZ	340	842[b]		325[b]		3.12
experiment [e]	318	792 ± 9		723		
NEO-MP2(ee+ep)[f]	334					
CC−VSCF-MP2[g]	327	811		925		

[a] Anharmonic contributions are critical for ν_3, the shared proton stretch. [b] Harmonic frequency corresponding to the optimized geometry. [c] From three-dimensional $1 \leftarrow 0$ eigenstate transitions. The potential energy surface for the eigenstates is obtained from a full scan of the quantum proton with the chlorides fixed at optimized geometry positions. Hence, the eigenstates here are corrected for anharmonicity but do not include coupling with the chloride motions. [d] For CCSD, the shared proton is not symmetrically placed along the Cl−Cl axis. This is in contrast with respect to all other optimized geometries here. [e] Reference 147. [f] Reproduced from ref 148. [g] Reproduced from ref 148 based on the implementation of VSCF by Gerber and co-workers.[60−62]

V. Vibrational Spectra of Clusters, Inclusive of Critical Nuclear Quantum Effects

As a benchmark of our method's accuracy, we examine the vibrational spectrum of $[Cl-H-Cl]^-$. To lay a foundation for the need for a dynamical study, we begin by examining at the harmonic frequencies calculated from optimized geometries, using various electronic structure methods in section VA. These results are compared with experiments, and the resultant deviations, due to anharmonicity, are then partially overcome using AIMD in section VB. Finally, in section VC, we provide results from QWAIMD, which provide enhanced agreement with the experimental results.

A. Harmonic Analysis of Cl−H−Cl$^-$. In Table 4, we present harmonic frequencies calculated from optimized geometries using a variety of electronic structure methods using both DFT and post-Hartree−Fock methods.

When comparing these calculations, it is interesting to note that all levels of electronic structure theory, except CCSD, predict equilibrium geometries where the shared proton is symmetrically arranged along the Cl−Cl axis. CCSD, on the contrary, predicts a geometry with the same symmetry to be a transition state with an imaginary frequency equal to 332i. The CCSD potential energy surface has a small (0.08 kcal/mol) barrier at the minimum geometry, which is an order of magnitude less than the zero-point energy (0.93 kcal/mol) of the same surface. As can be seen from Table 4, the proton stretch (ν_3) is not reproduced well enough by any of the electronic structure methods. This suggests a strong anharmonicity con-

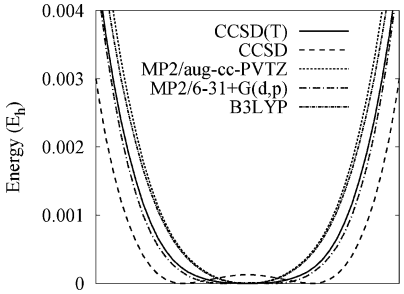

Figure 4. One-dimensional slices of the potential energy surfaces of the shared proton along the Cl−Cl axis at equilibrium geometries obtained at the levels of theory indicated in Table 4. The horizontal axis represents a spread of 0.529 Å (1 bohr). The B3LYP/aug-cc-PVTZ and B3LYP/6-31+G(d,p) surfaces are indistinguishable, and the CCSD surface shows a double well. The basis set used for both CCSD and CCSD(T) is aug-cc-PVTZ as listed in Table 4.

TABLE 5: Harmonic and Anharmonic Constants Calculated from the Eigenstates of the One-Dimensional Potentials

level of theory	w_e (cm^{-1})	w_ex_e (cm^{-1})	w_ey_e (cm^{-1})	w_ez_e (cm^{-1})
B3LYP/6-31+G(d,p)	827.54	−173.484	−11.0147	0.377976
B3LYP/aug-cc-PVTZ	833.463	−169.508	−10.7189	0.369335
MP2/6-31+G(d,p)	698.037	−217.648	−15.4189	0.553249
MP2/aug-cc-PVTZ	858.043	−181.427	−11.6547	0.402117
CCSD/aug-cc-PVTZ	565.65	−228.137	−16.9142	0.618542
CCSD(T)/aug-cc-PVTZ	730.253	−204.83	−14.3846	0.51683

tribution, as noted previously.[147] The proton potential energy surfaces shown in Figure 4 are obtained from retaining the Cl atoms at their respective optimized positions. A direct polynomial fit of these surfaces displays significant contributions from fourth- and sixth-order terms, which explains the limited accuracy of the harmonic frequency calculations shown in Table 4.

In fact, borrowing diatomic molecular spectroscopy notation, the harmonic w_e and anharmonic constants w_ex_e, w_ey_e, etc. for the ν_3 vibration at each level of theory can be calculated using the vibrational eigenstates determined from the Arnoldi diagonalization of these potential surfaces. The constants in Table 5 were determined from a least-squares fit of a fourth-order polynomial

$$G(\nu) = w_e\left(\nu+\frac{1}{2}\right) - w_ex_e\left(\nu+\frac{1}{2}\right)^2 + w_ey_e\left(\nu+\frac{1}{2}\right)^3 + w_ez_e\left(\nu+\frac{1}{2}\right)^4 \quad (14)$$

to the first 10 eigenstates of each one-dimensional potential energy surface shown in Figure 4. The anharmonic contributions are significant, and the first-order anharmonic constant, w_ex_e, is negative because the spacing between vibrational levels increases with respect to the harmonic approximation. In Table 4, we also provide corrections to the harmonic approximation by computing three-dimensional proton eigenstates at the equilibrium Cl−Cl geometries for the respective levels of theory. These eigenstates are obtained from Arnoldi diagonalization[156−158] of the three-dimensional proton potential surfaces obtained at the respective optimized geometries. (See footnote b in Table 4.) Even these calculations only provide an upper bound to the experimental results, although they significantly improve the quality of the spectra. Clearly, in addition to anharmonicity, coupling between the proton and the chloride motions is critical. This aspect also manifests itself through the relatively high

TABLE 6: Dynamically Averaged Vibrational Density of States Calculated from Classical aimd Studies

level of theory	temperature (K)[a]	ν_1 (cm^{-1})	ν_2 (cm^{-1})	ν_3 (cm^{-1})
B3LYP/6-31+G(d,p)	15.95	319	830	600
B3LYP/6-31+G(d,p)	50.29	308	818	658
B3LYP/6-31+G(d,p)	75.5	308	814	658
B3LYP/aug-cc-PVTZ	15.89	317	813	622
B3LYP/aug-cc-PVTZ	49.63	313	808	625
B3LYP/aug-cc-PVTZ	74.97	308	806	647
MP2/aug-cc-PVTZ	15.72	336	842	645
MP2/aug-cc-PVTZ	49.64	330	834	653
experiment [b]		318	792 ± 9	723

[a] Average internal temperature of the system during the simulation computed using nuclear velocities. [b] Reference 147.

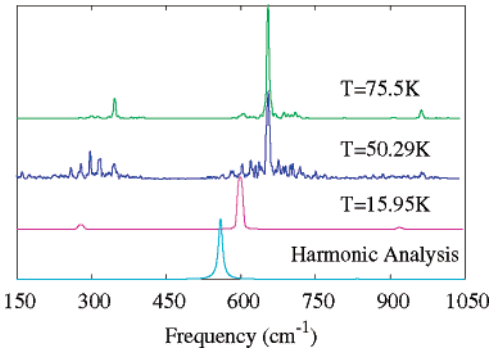

Figure 5. Dynamically averaged vibrational spectra obtained from classical AIMD simulations. See discussion for details.

degree of agreement between our three-dimensional proton eigenstate calculations in Table 4 and the correlation-corrected VSCF results for ν_3, reproduced from ref 148. The remainder of this publication deals with a discussion of improvements to ν_3 that arise by including the anharmonicity of the proton potential surface and the coupled motion of the shared proton and the chlorine atoms as allowed within classical AIMD and QWAIMD simulations.

B. Including Anharmonicity Contributions through Temperature-Dependent, Classical AIMD Simulations. It has been recently shown[9−11,13] that temperature-dependent AIMD techniques can accurately reproduce experimentally observed vibrational spectra even when harmonic analysis fails.[11,13,18] In Table 6 and Figure 5, we present our results from BOMD studies at constant energy (NVE) where spectra are computed using the Fourier transform of the dipole autocorrelation function (FT-DAC) and the velocity autocorrelation function (FT-VAC). While the FT-VAC strictly provides the vibrational density of states, the FT-DAC also accounts for dipole selection rules. Hence, the spectral intensities are generally expected to be different in the two cases. Deconvolving the FT-VAC spectra through analysis of the individual nuclear motions indicates temperature-dependent peaks corresponding to ν_1, ν_2, and ν_3. The dynamical spectra show an improvement in the ν_1 and ν_2 stretches over the harmonic approximation. The most dramatic change, however, is shown in the asymmetric proton stretch, ν_3.

To probe the effect of temperature, in Figure 6 we present the radial distribution functions for the proton position and Cl−Cl distances at different internal temperatures. The shared proton displays a broader distribution as the temperature increases. This is, however, coupled with a broader Cl−Cl distribution at higher temperatures. It is also important to note the transition in the proton radial distribution function from a bimodal distribution below 75 K to a single broad distribution at 150 K. At the lower

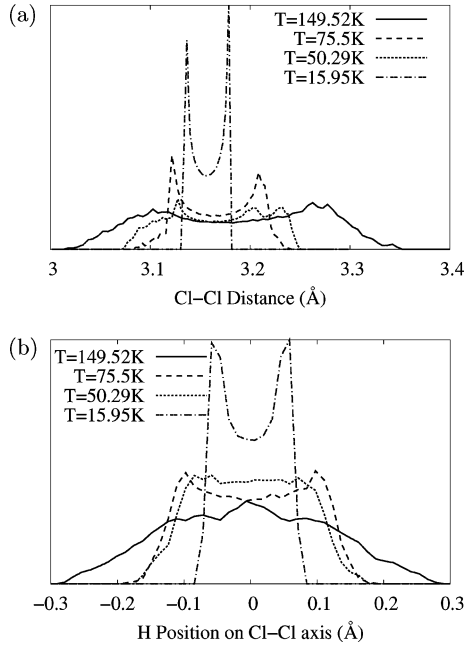

Figure 6. (a) Distribution of Cl−Cl distances and (b) hydrogen positions along the Cl−Cl axis for BOMD B3LYP/6-31+G(d,p) at several temperatures. Plots for other levels of theory and basis sets are similar.

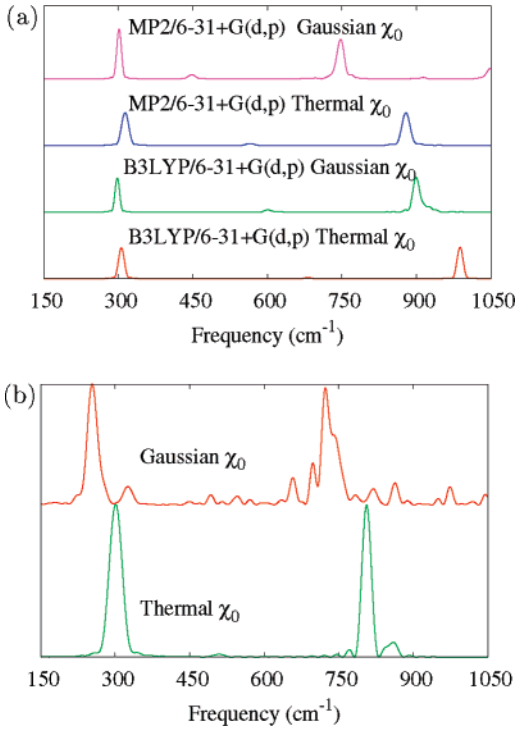

Figure 7. Fourier transform of the flux/velocity correlation function for (a) one- and (b) three-dimensional QWAIMD. The one-dimensional simulations ran for 2.5−4 ps, and the three-dimensional simulations ran for 1−2 ps. The prominent peaks in panel b are in close agreement with experiment.

temperatures, the average proton potential is a single well, while at high temperatures it tends to a double well, because larger Cl−Cl distances are sampled at higher temperatures. This changes the basic structure of the distribution and has a critical effect on the temperature dependence of the vibrational spectrum.

Due to a dependence of ν_3 on the simulation temperature, it is important to note that the experiments in ref 147 were performed using velocity modulation spectroscopy where the effective vibrational temperature could be as high as 1000 K.[159,160] Hence, it is not surprising that the higher-temperature AIMD results become closer to the experimental result. However, this also indicates an internal temperature dependence (and hence experimental technique dependence) to the spectrum, as has been noted for other fluxional systems.[10] It will be interesting to see how single-photon argon-tagged[161] and multiphoton experiments[25] differ in the prediction of the proton stretch for this particular system.

C. Quantum Wavepacket Description of the Vibrational Analysis. In this section, we present the vibrational density of states computed from QWAIMD simulations of $[Cl-H-Cl]^-$. As noted earlier, the FT-VAC represents the vibrational density of states. This aspect has been widely used in classical AIMD simulations.[9,11,13,162] Additionally, the FT-DAC provides the dipole selection rules. There exist many approaches that attempt to provide quantum corrections to such classical time-correlation functions.[163−165] Here, we present an alternate scheme to obtain the vibrational spectra directly from quantum−classical simulations such as those performed within QWAIMD.

In QWAIMD, the presence of both classical and quantum dynamical nuclei complicates the direct application of velocity correlation. We exploit the fact that the quantum correspondence for the classical nuclear velocity is given in terms of the probability flux or current[166]

$$\mathcal{J}(x,t) = \frac{\hbar}{2mi}[\psi^*(x,t)\nabla\psi(x,t) - \psi(x,t)\nabla\psi^*(x,t)]$$
$$= \frac{\hbar}{m}\,\mathrm{Im}[\psi^*(x,t)\nabla\psi(x,t)] \qquad (15)$$

where Im[A] represents the imaginary portion of the complex number A. Thus, to construct the velocity autocorrelation function, we consider the expectation value of flux at a given time

$$\mathbf{J}(t) = \langle\mathcal{J}\rangle = \mathcal{R}\left[\left\langle\psi(t)\middle|\frac{-i\hbar}{m}\nabla\middle|\psi(t)\right\rangle\right] \qquad (16)$$

in conjunction with the classical nuclear velocities. The symbol $\mathcal{R}[\cdots]$ represents the real part of the complex bracketed quantity.

Therefore, we simultaneously compute the correlation functions $\langle\mathbf{J}(t)\mathbf{J}(0)\rangle$ and $\langle v(t)v(0)\rangle$, and the full vibrational density of states is the Fourier transform of the cumulative flux/velocity correlation function

$$C(\omega) = \int_{-\infty}^{+\infty}\exp[-i\omega t]\{\langle v(t)v(0)\rangle_C + \langle\mathbf{J}(t)\mathbf{J}(0)\rangle_Q\} \qquad (17)$$

where the symbols $\langle\cdots\rangle_C$ and $\langle\cdots\rangle_Q$ represent the classical and quantum variable ensemble averages. It is also critical to note from eq 16 that for a simple Gaussian wavepacket the quantity $\langle\psi(t)|(-i\hbar/m)\nabla|\psi(t)\rangle$ is also equal to the transition dipole bracket and hence this quantity may contain some information also about the dipole selection rules in regions where semiclassical treatment is sufficient. This can be seen from the following analysis of eq 15 for time-independent Hamiltonians

TABLE 7: One- and Three-Dimensional QWAIMD Studies of the Vibrational Density of States as Calculated by the Flux/Velocity Correlation Function, Eq 17[a]

	temperature (K)[b]	χ_0	ν_1 (cm^{-1})	ν_3 (cm^{-1})		ν_2 (cm^{-1})	
1D-QWAIMD	133.76[c]	eq 12	301	988[d]	983[e]		
($N_Q = 101$; $N_E = 11$)	271.14[c]	eq 13	297	900[d]	920[e]		
	127.26[f]	eq 12	313	879[d]	876[e]		
	290.17[f]	eq 13	304	746[d]	764[e]		
3D-QWAIMD[g]	323.50	eq 12	300	806[d]	805[e]	857[d]	853[e]
($N_Q = 232\,897$[h]; $N_E = 343$)	714.45	eq 13	254	723[d]	739[e]	863[d]	858[e]
experiment[i]			318	723		792 ± 9	

[a] The assignments are confirmed by considering the dynamic average of the $1 \leftarrow 0$ eigenstate transitions. [b] Average internal temperature of the system during the simulation computed using nuclear velocities. [c] On-the-fly electronic structure is performed using B3LYP/6-31+G(d,p). [d] Obtained from the flux/velocity correlation function (eq 17). [e] Dynamically averaged $1 \leftarrow 0$ eigenstate transitions. [f] On-the-fly electronic structure is performed using MP2/6-31+G(d,p). [g] On-the-fly electronic structure is performed using B3LYP/6-31+G*. [h] $97 \times 49 \times 49$ grid with 97 grid points along the Cl−Cl axis. [i] Reference 147.

$$\mathscr{J}(x,t) = \frac{\hbar}{m}\,\mathrm{Im}[\psi^*(x,t)\nabla\psi(x,t)]$$
$$= \frac{\hbar}{m}\,\mathrm{Im}\left[\psi^*(x,0)\,\exp\left\{\frac{iHt}{\hbar}\right\}\nabla\,\exp\left\{-\frac{iHt}{\hbar}\right\}\psi(x,0)\right]$$
$$= \frac{\hbar}{m}\,\mathrm{Im}\left[\sum_i \phi_i^*\,\exp\left\{\frac{iE_it}{\hbar}\right\}\nabla\sum_j \exp\left\{-\frac{iE_jt}{\hbar}\right\}\phi_j\right] \quad (18)$$

Hence the Fourier transform of the expectation value of flux in eq 16, for time-independent Hamiltonians, can be written, using the convolution theorem,[146] as

$$\int_{-\infty}^{+\infty} dt\,\exp[-i\omega t]\{\langle \mathbf{J}(t)\mathbf{J}(0)\rangle_Q\} = \left|\int_{-\infty}^{+\infty} dt\,\exp[-i\omega t]\mathbf{J}(t)\right|^2$$
$$= \left|\int_{-\infty}^{+\infty} dt\,\exp[-i\omega t]\mathscr{R}\left[\sum_{i,j}\exp\left\{\frac{i(E_i - E_j)t}{\hbar}\right\}\frac{\langle\phi_i|\hat{\mathbf{p}}|\phi_j\rangle}{m}\right]\right|^2$$
$$= \left|\sum_{i,j}\delta\left(\omega - \frac{[E_i - E_j]}{\hbar}\right)\frac{\langle\phi_i|\hat{\mathbf{p}}|\phi_j\rangle}{m} + \delta\left(\omega - \frac{[E_j - E_i]}{\hbar}\right)\frac{\langle\phi_i|\hat{\mathbf{p}}|\phi_j\rangle^*}{m}\right|^2 \quad (19)$$

where $\delta(\cdots)$ is the Dirac delta function. Equation 19 clearly leads to a spectral representation with peaks positioned at the various energy differences that correspond to vibrational excitations. The situation for time-dependent Hamiltonians is, of course, complicated by the nature of the quantum−classical coupling. However, it is already clear from eq 19 that the peak intensities are proportional to the momentum of the wavepacket, which in turn is proportional to the transition dipole bracket in the semiclassical (Gaussian wavepacket) representation.

We present band assignments based on computation using eq 17 in Table 7 for two different temperatures for each level of theory. These are confirmed by calculating the average $1 \leftarrow 0$ transition energies over the course of a trajectory. As can be seen, the agreement between the 3D-QWAIMD results and experiment improves with increasing temperature. In addition, the high-temperature 3D-QWAIMD results for the shared proton stretch (ν_3) in this particular system seems to be in better agreement with experiment as compared to the implementation of correlation-corrected VSCF discussed in ref 148. The orthogonal motion of the shared proton (ν_2), on the contrary, is not in agreement to the same extent as the classical AIMD simulations described in Table 6, due to the sparse grid utilized in this direction (97 grid points along the Cl−Cl axis and 49 grid points in the orthogonal direction; see Table 6 for details).

It is critical to distinguish the trends in the change in the ν_3 peaks for the classical and quantum wavepacket AIMD simulations. As discussed in section VB and shown in Figure 6, an increase in temperature for the classical spectra allows the system to sample larger Cl−Cl distances. This applies to QWAIMD as well. But the effect of temperature on ν_3 is different for the classical and quantum simulations. In classical AIMD, the proton dynamics are influenced by the increasing fourth- and sixth-order terms in the potential surface on account of the larger Cl−Cl distances sampled. These steeper turning points, sampled at higher temperatures by the classical proton (Figure 6), blue-shift the proton stretch peak. For QWAIMD, on the contrary, the ν_3 peak is red-shifted at higher temperatures, because the potential surface becomes wider due to the increasing higher-order terms and larger Cl−Cl distances sampled. The flatter average potential results in a decrease in the $1 \leftarrow 0$ transition energy for one- and three-dimensional simulations. Hence, the effect of temperature on the quantum treatment is quite different from that obtained from the classical treatment. However, the two types of calculated spectra in this study tend to converge to the experimental (high-temperature) spectrum. In addition, the difference between one- and three-dimensional QWAIMD simulations for ν_3 is significant for this case. Dimensional confinement blue-shifts the frequencies as is to be expected.

VI. Concluding Remarks

In this paper, we have extended the recently developed quantum wavepacket ab initio molecular dynamics technique that allows simultaneous quantum−classical dynamics of electrons and nuclei. Modifications to the computational scheme through the utilization of wavelet theory and the use of low-pass filtered Lagrange interpolating polynomials renders the approach robust, accurate, and computationally efficient.

We have demonstrated one application of our approach through an analysis of the rovibrationalspectroscopy in a small $Cl{-}H{-}Cl^-$ cluster. This problem has been studied by a number of theoretical and experimental groups. To study rovibrational spectroscopy in such clusters, we have employed a novel, cumulative flux/velocity correlation function where the wavepacket flux is combined with the classical nuclear velocities to obtain a general description of vibrational density of states in quantum−classical systems. The approach is analytically shown to be exact for time-independent Hamiltonians, and numerical

demonstrations are provided for the case of time-dependent Hamiltonians, which corresponds to the situation in QWAIMD.

The $Cl-H-Cl^-$ cluster is interesting because Harmonic frequencies obtained even from very high levels of ab initio quantum chemical calculations are in wide disagreement with experiment. We study this system using multiple methods, including post-Hartree−Fock electronic structure optimization and harmonic frequency calculations, the application of classical ab initio molecular dynamics techniques to account for anharmonicities in the potential, and finally by using quantum wavepacket ab initio dynamics. In addition, we also perform corrections to post-Hartree−Fock and DFT harmonic frequencies by including critical quantum nuclear effects, which dramatically improve the level of agreement with experiment in all of these cases. We generally find that classical ab initio molecular dynamics employing DFT, in this case, monotonically improves over the harmonic frequencies in the direction of the experimental result, with increasing classical temperature (computed using classical nuclear velocities). The high-temperature ab initio molecular dynamics results are closer to being in agreement with experiment as compared to the harmonic results. This is explained by noting that at higher temperatures the classical proton samples steeper turning points, because the potential becomes increasingly dominated by fourth- and sixth-order terms as the chlorides sample larger distances. This effectively blue-shifts the proton stretch with increasing temperature. We keep these comparisons for the different temperatures meaningful by noting the high vibrational temperature involved in the experimental situation.

The utilization of QWAIMD brings our final results very close to those experimentally obtained. Here again, there is a temperature dependence to our results on account of two factors. While for the classically treated nuclei the effect of temperature affects the kinetic energies and hence the sampling of the potential energy surface, for the quantum mechanically treated nuclei (through wavepackets) the initial temperature affects the populations of the eigenstates belonging to the quantized particle in the initial wavepacket. Hence, the dynamical evolution of high- and low-temperature wavepackets can be different through the occurrence of hot bands. But, in addition, the dynamical evolution of the wavepacket is closely connected to the temperature-dependent sampling performed by the classical nuclei, which again has an effect on the result.

In this paper, we have also utilized the Bohmian quantum potential as a tool to understand the connections between wavepacket AIMD and classical AIMD simulations. Such tools are critical because they allow us to determine the extent to which quantum dynamics plays a role. We will consider these in greater detail in future publications.

Acknowledgment. This research is funded by the Camille and Henry Dreyfus Foundation, the Arnold and Mabel Beckman Foundation, and Indiana University. The authors thank Professor Krishnan Raghavachari for useful discussions, and acknowledgment is also due to Xiaohu Li, who helped complete the paper. I.S. thanks Dr. Jacek Jakowski for useful discussions.

References and Notes

(1) Haile, S. M.; Boysen, D. A.; Chisholm, C. R. I.; Merle, R. B. *Nature* **2001**, *410*, 910.
(2) Schuster, M. F.; Meyer, W. H. *Annu. Rev. Mater. Res.* **2003**, *33*, 233−261.
(3) Kreuer, K. D.; Fuchs, A.; Ise, M.; Spaeth, M.; Maier, J. *Electrochim. Acta* **1998**, *43*, 1281−1288.
(4) Iannuzzi, M.; Parrinello, M. *Phys. Rev. Lett.* **2004**, *93*, 025901.
(5) Hudson, B. S.; Verdal, N. *Physica B* **2006**, *385*, 212−215.
(6) Gertner, B. J.; Hynes, J. T. *Science* **1996**, *271*, 1563−1566.
(7) Devlin, J. P.; Uras, N.; Sadlej, J.; Buch, V. *Nature* **2002**, *417*, 269−271.
(8) Aloisio, S.; Francisco, J. S. *Acc. Chem. Res.* **2000**, *33*, 825−830.
(9) Iyengar, S. S. *J. Chem. Phys.* **2005**, *123*, 084310.
(10) Li, X.; Teige, V. E.; Iyengar, S. S. *J. Phys. Chem. A* **2007**, *111*, 4815−4820.
(11) Iyengar, S. S. *J. Chem. Phys.* **2007**, *126*, 216101.
(12) Iyengar, S. S.; Day, T. J. F.; Voth, G. A. *Int. J. Mass Spectrom.* **2005**, *241*, 197−204.
(13) Iyengar, S. S.; Petersen, M. K.; Day, T. J. F.; Burnham, C. J.; Teige, V. E.; Voth, G. A. *J. Chem. Phys.* **2005**, *123*, 084309.
(14) Petersen, M. K.; Iyengar, S. S.; Day, T. J. F.; Voth, G. A. *J. Phys. Chem. B* **2004**, *108*, 14804−14806.
(15) Marx, D.; Tuckerman, M. E.; Hutter, J.; Parrinello, M. *Nature* **1999**, *397*, 601.
(16) Tuckerman, M. E.; Marx, D.; Parrinello, M. *Nature* **2002**, *417*, 925−929.
(17) Asthagiri, D.; Pratt, L. R.; Kress, J. D.; Gomez, M. A. *Proc. Natl. Acad. Sci. U.S.A.* **2004**, *101*, 7229−7233.
(18) Shin, J.-W.; Hammer, N. I.; Diken, E. G.; Johnson, M. A.; Walters, R. S.; Jaeger, T. D.; Duncan, M. A.; Christie, R. A.; Jordan, K. D. *Science* **2004**, *304*, 1137−1140.
(19) Hammer, N. I.; Diken, E. G.; Roscioli, J. R.; Johnson, M. A.; Myshakin, E. M.; Jordan, K. D.; McCoy, A. B.; Huang, X.; Bowman, J. M.; Carter, S. *J. Chem. Phys.* **2005**, *122*, 244301.
(20) Diken, E. G.; Headrick, J. M.; Roscioli, J. R.; Bopp, J. C.; Johnson, M. A.; McCoy, A. B. *J. Phys. Chem. A* **2005**, *109*, 1487−1490.
(21) Nagel, Z.; Klinman, J. *Chem. Rev.* **2006**, *106*, 3095−3118.
(22) Cleland, W. W.; Kreevoy, M. M. *Science* **1994**, *264*, 1887.
(23) Warshel, A.; Papazyan, A.; Kollman, P. A. *Science* **1995**, *269*, 102.
(24) Roscioli, J. R.; McCunn, L. R.; Johnson, M. A. *Science* **2007**, *316*, 249−254.
(25) Moore, D. T.; Oomens, J.; van der Meer, L.; von Helden, G.; Meijer, G.; Valle, J.; Marshall, A. G.; Eyler, J. R. *ChemPhysChem* **2004**, *5*, 740−743.
(26) Rubtsov, I. V.; Hochstrasser, R. M. *J. Phys. Chem. B* **2002**, *106*, 9165.
(27) Rector, K. D.; Zimdars, D.; Fayer, M. D. *J. Chem. Phys.* **1998**, *109*, 5455.
(28) *Dynamics of Molecules and Chemical Reactions*; Wyatt, R. E., Zhang, J. Z. H., Eds.; Marcel Dekker: New York, 1996.
(29) Bowman, J. M. *Acc. Chem. Res.* **1986**, *19*, 202−208.
(30) McCoy, A. B.; Gerber, R. B.; Ratner, M. A. *J. Chem. Phys* **1994**, *101*, 1975.
(31) McCoy, A. B.; Huang, X.; Carter, S.; Bowman, J. M. *J. Chem. Phys.* **2005**, *123*, 064317.
(32) Iyengar, S. S.; Parker, G. A.; Kouri, D. J.; Hoffman, D. K. *J. Chem. Phys.* **1999**, *110*, 10283−10298.
(33) Meyer, H.-D.; Manthe, U.; Cederbaum, L. S. *Chem. Phys. Lett.* **1990**, *165*, 73.
(34) Lopreore, C. L.; Wyatt, R. E. *Phys. Rev. Lett.* **1999**, *82*, 5190.
(35) Schatz, G. C.; Kupperman, A. *J. Chem. Phys.* **1976**, *65*, 4642.
(36) Delos, J. B. *Rev. Mod. Phys.* **1981**, *53*, 287.
(37) Feit, M. D.; Fleck, J. A. *J. Chem. Phys.* **1982**, *78*, 301.
(38) Kosloff, R. *Annu. Rev. Phys. Chem.* **1994**, *45*, 145.
(39) Leforestier, C.; Bisseling, R. H.; Cerjan, C.; Feit, M. D.; Freisner, R.; Guldberg, A.; Hammerich, A.; Jolicard, D.; Karrlein, W.; Meyer, H. D.; Lipkin, N.; Roncero, O.; Kosloff, R. *J. Comput. Phys.* **1991**, *94*, 59.
(40) DeVries, P. In *Atomic and Molecular Processes with Short Intense Laser Pulses*, Bandrauk, A. D., Ed.; NATO ASI Series B, Physics 171; Plenum Press: New York, 1988; p 481.
(41) Jang, H. W.; Light, J. C. *J. Chem. Phys.* **1995**, *102*, 3262−3268.
(42) Althorpe, S. C.; Clary, D. C. *Annu. Rev. Phys. Chem.* **2003**, *54*, 493−529.
(43) Althorpe, S. C.; Fernandez-Alonso, F.; Bean, B. D.; Ayers, J. D.; Pomerantz, A. E.; Zare, R. N.; Wrede, E. *Nature* **2002**, *416*, 67−70.
(44) Huang, Y.; Iyengar, S. S.; Kouri, D. J.; Hoffman, D. K. *J. Chem. Phys.* **1996**, *105*, 927.
(45) Miller, W. H.; Schwartz, S. D.; Tromp, J. W. *J. Chem. Phys.* **1983**, *79*, 4889.
(46) Makri, N. *Comput. Phys. Commun.* **1991**, *63*, 389−414.
(47) Cao, J.; Voth, G. A. *J. Chem. Phys.* **1994**, *100*, 5106.
(48) Jang, S.; Voth, G. A. *J. Chem. Phys.* **1999**, *111*, 2357.
(49) Feit, M. D.; Fleck, J. A. *J. Chem. Phys.* **1983**, *79*, 301.
(50) Feit, M. D.; Fleck, J. A. *J. Chem. Phys.* **1984**, *80*, 2578.
(51) Kosloff, D.; Kosloff, R. *J. Comput. Phys.* **1983**, *52*, 35.
(52) Kosloff, D.; Kosloff, R. *J. Chem. Phys.* **1983**, *79*, 1823.
(53) Tal-Ezer, H.; Kosloff, R. *J. Chem. Phys.* **1984**, *81*, 3967.
(54) Hartke, B.; Kosloff, R.; Ruhman, S. *Chem. Phys. Lett.* **1986**, *158*, 223.
(55) Iyengar, S. S.; Kouri, D. J.; Hoffman, D. K. *Theor. Chem. Acc.* **2000**, *104*, 471.

(56) Lill, J. V.; Parker, G. A.; Light, J. C. *Chem. Phys. Lett.* **1982**, *89*, 483.
(57) Light, J. C.; Hamilton, I. P.; Lill, J. V. *J. Chem. Phys.* **1985**, *82*, 1400.
(58) Colbert, D. T.; Miller, W. H. *J. Chem. Phys.* **1992**, *96*, 1982−1991.
(59) Huang, Y.; Kouri, D. J.; Arnold, M.; Thomas, Marchioro, L., I.; Hoffman, D. K. *Comput. Phys. Commun.* **1994**, *80*, 1.
(60) Gerber, R. B.; Ratner, M. A. *J. Chem. Phys.* **1988**, *70*, 97−132.
(61) Jung, J. O.; Gerber, R. B. *J. Chem. Phys.* **1996**, *105*, 10332.
(62) Matsunaga, N.; Chaban, G. M.; Gerber, R. B. *J. Chem. Phys.* **2002**, *117*, 3541.
(63) Deumens, E.; Diz, A.; Longo, R.; Öhrn, Y. *Rev. Mod. Phys.* **1994**, *66*, 917.
(64) Hack, M. D.; Truhlar, D. G. *J. Phys. Chem. A* **2000**, *104*, 7917−7926.
(65) Jasper, A. W.; Zhu, C.; Nangia, S.; Truhlar, D. G. *Faraday Discuss.* **2004**, *127*, 1−22.
(66) Miller, W. H. *J. Phys. Chem. A* **2001**, *105*, 2942−2955.
(67) Heller, E. J. *J. Chem. Phys.* **1975**, *62*, 1544−1555.
(68) Fiete, G. A.; Heller, E. J. *Phys. Rev. A* **2003**, *68*, 022112.
(69) Hammes-Schiffer, S.; Tully, J. *J. Chem. Phys.* **1994**, *101*, 4657−4667.
(70) Ben-Nun, M.; Quenneville, J.; Martínez, T. J. *J. Phys. Chem. A* **2000**, *104*, 5161.
(71) Coe, J. D.; Martinez, T. J. *J. Am. Chem. Soc.* **2005**, *127*, 4560.
(72) Martinez, T. J.; Ben-Nun, M.; Ashkenazi, G. *J. Chem. Phys.* **1996**, *104*, 2847.
(73) Martinez, T. J.; Levine, R. D. *J. Chem. Phys.* **1996**, *105*, 6334.
(74) Micha, D. A. *J. Phys. Chem. A* **1999**, *103*, 7562−7574.
(75) Gerber, R. B.; Buch, V.; Ratner, M. A. *J. Chem. Phys.* **1982**, *77*, 3022.
(76) Bisseling, R. H.; Kosloff, R.; Gerber, R. B.; Ratner, M. A.; Gibson, L.; Cerjan, C. *J. Chem. Phys.* **1987**, *87*, 2760−2765.
(77) Makri, N.; Miller, W. H. *J. Chem. Phys.* **1987**, *87*, 5781−5787.
(78) McCoy, A. B. *Mol. Phys.* **1995**, *85*, 965.
(79) Wang, I. S. Y.; Karplus, M. *J. Am. Chem. Soc.* **1973**, *95*, 8160.
(80) Leforestier, C. *J. Chem. Phys.* **1978**, *68*, 4406.
(81) Car, R.; Parrinello, M. *Phys. Rev. Lett.* **1985**, *55*, 2471.
(82) Payne, M. C.; Teter, M. P.; Allan, D. C.; Arias, T. A.; Joannopoulos, J. D. *Rev. Mod. Phys.* **1992**, *64*, 1045.
(83) Schlegel, H. B.; Millam, J. M.; Iyengar, S. S.; Voth, G. A.; Daniels, A. D.; Scuseria, G. E.; Frisch, M. J. *J. Chem. Phys.* **2001**, *114*, 9758.
(84) Marx, D.; Hutter, J. Ab initio molecular dynamics: Theory and implementation. In *Modern Methods and Algorithms of Quantum Chemistry: Proceedings*, 2nd ed.; NIC Series 3; John von Neumann Institute for Computing: Jülich, Switzerland, 2000; pp 301−449.
(85) Bolton, K.; Hase, W. L.; Peslherbe, G. H. Direct dynamics of reactive systems. In *Modern Methods for Multidimensional Dynamics Computations in Chemistry*; World Scientific: Singapore, 1998; pp 143−189.
(86) Schlegel, H. B. *J. Comput. Chem.* **2003**, *24*, 1514−1527.
(87) Peng, T.; Zhang, J. Z. H. *J. Chem. Phys.* **1996**, *105*, 6072−6074.
(88) Althorpe, S. C. *J. Chem. Phys.* **2001**, *114*, 1601−1616.
(89) Hirschfelder, J. O.; Dahler, J. S. *Proc. Natl. Acad. Sci. U.S.A.* **1956**, *42*, 363.
(90) Delves, L. M. *Nucl. Phys.* **1959**, *9*, 391.
(91) Pack, R. T.; Parker, G. A. *J. Chem. Phys.* **1987**, *87*, 3888.
(92) Skone, J. H.; Pak, M. V.; Hammes-Schiffer, S. *J. Chem. Phys.* **2005**, *123*, 134108.
(93) Lester, W. A., Jr.; Hammond, B. L. *Annu. Revs. Phys. Chem.* **1990**, *41*, 283−311.
(94) Pak, M. V.; Chakraborty, A.; Hammes-Schiffer, S. *J. Phys. Chem. A* **2007**, *111*, 4522.
(95) Smith, F. T. *J. Math. Phys.* **1962**, *3*, 735.
(96) Carter, S.; Bowman, J. M. *J. Chem. Phys.* **1998**, *108*, 4397−4404.
(97) Iyengar, S. S.; Jakowski, J. *J. Chem. Phys.* **2005**, *122*, 114105.
(98) Iyengar, S. S. *Theor. Chem. Acc.* **2006**, *116*, 326.
(99) Jakowski, J.; Sumner, I.; Iyengar, S. S. *J. Chem. Theory Comput.* **2006**, *2*, 1203−1219.
(100) Tully, J. C. *Faraday Discuss.* **1998**, *110*, 407 − 419.
(101) Kapral, R.; Ciccotti, G. *J. Chem. Phys.* **1999**, *110*, 8919.
(102) Horenko, I.; Salzmann, C.; Schmidt, B.; Schutte, C. *J. Chem. Phys.* **2002**, *117*, 11075−11088.
(103) Donoso, A.; Zheng, Y. J.; Martens, C. C. *J. Chem. Phys.* **2003**, *119*, 5010.
(104) Brooksby, C.; Prezhdo, O. V. *Chem. Phys. Lett.* **2001**, *346*, 463−469.
(105) Prezhdo, O. V.; Brooksby, C. *Phys. Rev. Lett.* **2000**, *86*, 3215−3219.
(106) Gindensperger, E.; Meier, C.; Beswick, J. A. *J. Chem. Phys.* **2000**, *113*, 9369.
(107) Remler, D. K.; Madden, P. A. *Mol. Phys* **1990**, *70*, 921.
(108) Iyengar, S. S.; Schlegel, H. B.; Millam, J. M.; Voth, G. A.; Scuseria, G. E.; Frisch, M. J. *J. Chem. Phys.* **2001**, *115*, 10291.
(109) Schlegel, H. B.; Iyengar, S. S.; Li, X.; Millam, J. M.; Voth, G. A.; Scuseria, G. E.; Frisch, M. J. *J. Chem. Phys.* **2002**, *117*, 8694.
(110) Iyengar, S. S.; Schlegel, H. B.; Voth, G. A.; Millam, J. M.; Scuseria, G. E.; Frisch, M. J. *Isr. J. Chem.* **2002**, *42*, 191−202.
(111) Iyengar, S. S.; Frisch, M. J. *J. Chem. Phys.* **2004**, *121*, 5061.
(112) Li, X.; Iyengar, S. S., to be submitted for publication.
(113) Iyengar, S. S.; Jakowski, J.; Sumner, I., to be submitted for publication.
(114) Grossman, A.; Morlet, J. *SIAM J. Math. Anal.* **1984**, *15*, 723.
(115) Strang, G. *SIAM Rev.* **1989**, *31*, 613−627.
(116) Strang, G.; Nguyen, T. *Wavelets and Filter Banks*; Wellesley-Cambridge Press: Wellesley, MA, 1996.
(117) Daubechies, I. *Ten Lectures in Wavelets*; Society for Industrial and Applied Mathematics: Philadelphia, PA, 1992.
(118) Wei, G. W.; Zhang, D. S.; Kouri, D. J.and Hoffman, D. K. *Phys. Rev. Lett.* **1997**, *79*, 775.
(119) Madelung, E. *Z. Phys.* **1926**, *40*, 322−326.
(120) de Broglie, L. *An Introduction to the Study of Wave Mechanics*; E. P. Dutton and Company: New York, 1930.
(121) Bohm, D. *Phys. Rev.* **1952**, *85*, 166.
(122) *Bohmian Mechanics and Quantum Theory: An Appraisal*; Cushing, J. T., Fine, A., Goldstein, S., Eds.; Kluwer Academic Publishers: Boston, 1996.
(123) Holland, P. R. *The Quantum Theory of Motion*; Cambridge University Press: New York, 1993.
(124) Wyatt, R. E. *J. Chem. Phys.* **1999**, *111*, 4406.
(125) Day, B. K.; Askar, A.; Rabitz, H. A. *J. Chem. Phys.* **1998**, *109*, 8770.
(126) Garashchuk, S.; Rassolov, V. A. *Chem. Phys. Lett.* **2002**, *364*, 562−567.
(127) Gibson, D. A.; Ionova, I. V.; Carter, E. A. *Chem. Phys. Lett.* **1995**, *240*, 261.
(128) Ehrenfest, P. *Z. Phys.* **1927**, *45*, 455.
(129) Iyengar, S. S.; Schlegel, H. B.; Voth, G. A. *J. Phys. Chem. A* **2003**, *107*, 7269−7277.
(130) Rega, N.; Iyengar, S. S.; Voth, G. A.; Schlegel, H. B.; Vreven, T.; Frisch, M. J. *J. Phys. Chem. B* **2004**, *108*, 4210−4220.
(131) Tangney, P.; Scandolo, S. *J. Chem. Phys.* **2002**, *116*, 14.
(132) Andersen, H. C. *J. Chem. Phys.* **1980**, *72*, 2384−2393.
(133) Parrinello, M.; Rahman, A. *Phys. Rev. Lett.* **1980**, *45*, 1196−1199.
(134) Trotter, M. F. *Proc. Am. Math. Soc.* **1959**, *10*, 545.
(135) Nelson, E. *J. Math. Phys.* **1964**, *5*, 332.
(136) Strang, G. *SIAM J. Numer. Anal.* **1968**, *5*, 506−516.
(137) Kouri, D. J.; Huang, Y.; Hoffman, D. K. *Phys. Rev. Lett.* **1995**, *75*, 49−52.
(138) Hoffman, D. K.; Nayar, N.; Sharafeddin, O. A.; Kouri, D. J. *J. Phys. Chem.* **1991**, *95*, 8299.
(139) Swope, W. C.; Andersen, H. C.; Berens, P. H.; Wilson, K. R. *J. Chem. Phys.* **1982**, *76*, 637.
(140) Strang, G.; Strela, V. *Opt. Eng.* **1994**, *33*, 2104−2107.
(141) Chan, Y. T. *Wavelet Basics*; Kluwer Academic Publishers: Boston, 1995.
(142) Johnson, B. R.; Modisette, J. P.; Nordlander, P. J.; Kinsey, J. L. *J. Chem. Phys.* **1999**, *110*, 8309−8317.
(143) Hoffman, D. K.; Wei, G. W.; Zhang, D. S.; Kouri, D. J. *Phys. Rev. E* **1998**, *57*, 6152−6160.
(144) Arias, T. *Rev. Mod. Phys.* **1999**, *71*, 267−311.
(145) Goedecker, S. *Rev. Mod. Phys.* **1999**, *71*, 1085.
(146) Press, W. H.; Teukolsky, S. A.; Vetterling, W. T.; Flannery, B. P. *Numerical Recipes in C*, 2nd ed.; Cambridge University Press: New York, 1992.
(147) Kawaguchi, K. *J. Chem. Phys* **1988**, *88*, 4186−4189.
(148) Swalina, C.; Hammes-Schiffer, S. *J. Phys. Chem. A* **2005**, *109*, 10410.
(149) McCoy, A. B. *J. Chem. Phys.* **1995**, *103*, 986.
(150) Botschwina, P.; Sebal, P.; Burmeister, R. *J. Chem. Phys.* **1988**, *88*, 5246.
(151) Metz, R. B.; Kitsopoulos, T.; Weaver, A.; Neumark, D. *J. Chem. Phys.* **1988**, *88*, 1463.
(152) Swalina, C.; Pak, M. V.; Hammes-Schiffer, S. *Chem. Phys. Lett.* **2005**, *404*, 394.
(153) Del Popolo, M. G.; Kohanoff, J.; Lynden-Bell, R. M. *J. Phys. Chem. B* **2006**, *110*, 8798.
(154) Mo, O.; Yanez, M.; Del Bene, J. E.; Alkorta, L.; Elguero, J. *ChemPhysChem* **2005**, *6*, 1411.
(155) Frisch, M. J.; Trucks, G. W.; Schlegel, H. B.; Scuseria, G. E.; Robb, M. A.; Cheeseman, J. R.; Montgomery, Jr., J. A.; Vreven, T.; Kudin, K. N.; Burant, J. C.; Millam, J. M.; Iyengar, S. S.; Tomasi, J.; Barone, V.; Mennucci, B.; Cossi, M.; Scalmani, G.; Rega, N.; Petersson, G. A.; Nakatsuji, H.; Hada, M.; Ehara, M.; Toyota, K.; Fukuda, R.; Hasegawa, J.;

Ishida, M.; Nakajima, T.; Honda, Y.; Kitao, O.; Nakai, H.; Klene, M.; Li, X.; Knox, J. E.; Hratchian, H. P.; Cross, J. B.; Adamo, C.; Jaramillo, J.; Gomperts, R.; Stratmann, R. E.; Yazyev, O.; Austin, A. J.; Cammi, R.; Pomelli, C.; Ochterski, J. W.; Ayala, P. Y.; Morokuma, K.; Voth, G. A.; Salvador, P.; Dannenberg, J. J.; Zakrzewski, V. G.; Dapprich, S.; Daniels, A. D.; Strain, M. C.; Farkas, O.; Malick, D. K.; Rabuck, A. D.; Raghavachari, K.; Foresman, J. B.; Ortiz, J. V.; Cui, Q.; Baboul, A. G.; Clifford, S.; Cioslowski, J.; Stefanov, B. B.; Liu, G.; Liashenko, A.; Piskorz, P.; Komaromi, I.; Martin, R. L.; Fox, D. J.; Keith, T.; Al-Laham, M. A.; Peng, C. Y.; Nanayakkara, A.; Challacombe, M.; Gill, P. M. W.; Johnson, B.; Chen, W.; Wong, M. W.; Gonzalez, C.; Pople, J. A. *Gaussian Development Version*, revision B.01; Gaussian, Inc.: Pittsburgh PA.

(156) Golub, G. H.; van Loan, C. F. *Matrix Computations*, 3rd ed.; Johns Hopkins University Press: Baltimore, MD, 1996.

(157) Sorensen, D. C. *SIAM J. Matris Anal. Appl.* **1992**, *13*, 357−385.

(158) Parlett, B. N.; Saad, Y. *Linear Algebra Appl.* **1987**, *88/89*, 575−595.

(159) Gudeman, C.; Begemann, M.; Pfaff, J.; R.J.Saykally. *Phys. Rev. Lett.* **1983**, *50*, 727.

(160) Saykally, R. *Science* **1988**, *239*, 157.

(161) Diken, E. G.; Headrick, J. M.; Roscioli, J. R.; Bopp, J. C.; Johnson, M. A.; McCoy, A. B. *J. Phys. Chem. A* **2005**, *109*, 1487−1490.

(162) Laasonen, K.; Sprik, M.; Parrinello, M.; Car, R. *J. Chem. Phys.* **1993**, *99*, 9080−9089.

(163) Berens, P. H.; White, S. R.; Wilson, K. R. *J. Chem. Phys.* **1981**, *75*, 515.

(164) Bader, J. S.; Berne, B. J. *J. Chem. Phys.* **1994**, *100*, 8359.

(165) Lawrence, C. P.; Nakayama, A.; Makri, N.; Skinner, J. L. *J. Chem. Phys.* **2004**, *120*, 6621.

(166) Sakurai, J. J. *Modern Quantum Mechanics*; Addison-Wesley: Reading, MA, 1994.

(167) For a detailed discussion on the connections between multiwavelets[140] and the Gaussian basis functions commonly used in electronic structure, see ref. 111.